UCLA
UCLA Electronic Theses and Dissertations

Title

Improved Deposition Techniques of Tin Oxide Thin Films for Developing High-Performance Perovskite Solar Cells

Permalink

https://escholarship.org/uc/item/6hv847v4

Author

Shrote, Vinayak

Publication Date

2023

Peer reviewed|Thesis/dissertation

UNIVERSITY OF CALIFORNIA

Los Angeles

Improved Deposition Techniques of Tin Oxide Thin Films for Developing High-Performance

Perovskite Solar Cells

A thesis submitted in partial satisfaction of the requirements for the degree Master of Science

in Materials Science and Engineering

by

Vinayak Shrote

2023

ABSTRACT OF THE THESIS

Improved Deposition Techniques of Tin Oxide Thin Films for Developing Efficient

Perovskite Solar Cells

by

Vinayak Shrote

Master of Science in Materials Science and Engineering

University of California, Los Angeles, 2023

Professor Yang Yang, Chair

Inorganic lead halide perovskite solar cells have emerged as a promising photovoltaic technology with their immense potential to consistently deliver high power output. This has been attributed to the unique electronic and optical properties of the perovskite and the carrier transport films. As a result, these devices possess power conversion efficiencies that vigorously compete with those of standard silicon solar cells. However, certain challenges prevent the commercialization of this technology. Existing methodologies for fabricating the carrier transport layers result in films with high defect densities that affect the device's performance.

In this work, we report the fabrication of the electron-selective layers for highly efficient perovskite solar cells via chemical bath deposition and sputter deposition. Improved process controls over the chemical bath deposition technique yielded highly efficient devices with a champion power conversion efficiency of 23.8%.

The thesis of Vinayak Shrote is approved.

Yinmin Wang

Jaime Marian

Yang Yang, Committee Chair

University of California, Los Angeles

2023

Dedicated to my family

TABLE OF CONTENTS

LIST OF FIGURES

LIST OF TABLES

ACKNOWLEDGEMENTS

I would like to express my deepest gratitude to my supervisor, Prof. Yang Yang, for giving me the magnificent opportunity to contribute meaningfully to his group. It was an honor to work under his distinguished guidance and support throughout my program. I am very thankful to my committee members, Prof. Jaime Marian and Prof. Yinmin Morris Wang, for the insightful reviews and suggestions they provided in the development of this thesis report.

Furthermore, I extend my greatest gratitude to my Qiyu Xing and Yepin Zhao for their unwavering mentorship and support which helped to bring this research to a fruitful completion. Their insightful suggestions and persistent support were key contributing factors to the development of this research.

I am also very thankful for the research infrastructure provided by the UCLA Nanofabrication Laboratory (NanoLab) which bolstered this research. I am also thankful to its distinguished staff for providing me with their valuable assistance and support while leveraging the NanoLab resources.

I am deeply indebted to my colleagues, Wenxin Yang, Haoxiang Duan, and Jonah Yang, for their collective assistance in building this work. Their valuable inputs on data processing proved extremely useful in presenting this work.

I offer my greatest thanks to Nikhil Choudhary and Harshal Sonagara for constantly supporting me during my time at UCLA.

Finally, I am grateful to my parents and family for their unparalleled support and love, which were key driving factors toward the completion of my program at UCLA.

CHAPTER 1: INTRODUCTION

A significant challenge that several industries throughout the globe face today is the rapidly increasing demand for energy to drive their critical operations coupled with an equal and imposing demand from the population to transition to cleaner and safer resources from which this energy can be extracted. While there exist several sustainable energy practices that leverage natural resources, solar energy is one such resource that has found a broad interest among several laboratories and industries across the globe. Since then, photovoltaic technology has been experiencing staggering growth owing to novel developments in solar cell research.

1.1 State of the art of photovoltaic technologies:

Solar cell technologies have been prevalent in the globe since the 1950s, with the first solar cell developed by Chapin et al in 1954, at Bell Labs[1]. Since then, numerous developments have been initiated to develop these technologies further. The most commonplace and widely commercialized one is the conventional crystalline silicon solar cell, which finds use in almost every solar application to date. Other prevalent and emerging technologies include Copper Indium Gallium Selenide (CIGS), GaAs, CdTe, Dye-sensitized Solar Cells (DSSCs), and perovskite solar cells [2–7]. Of particular interest in the category of perovskite solar cells is the inorganic-organic lead halide perovskites. These are particularly promising due to their potential to deliver enhanced efficiencies due to their unique optoelectronic properties such as high absorption coefficient, long carrier diffusion length, low defect density, tunable bandgap, low recombination rate, and high mobility of charge carriers[8].

1.1.1 Key Parameters for evaluating device performance:

When assessing the overall performance of solar cell devices, two critical factors must be taken into consideration: the power conversion efficiency (PCE) of the device and the stability of the device. The PCE of a cell is a measure of the energy output of the cell and demonstrates the percentage of incident solar power that is converted to usable electricity output. The stability of the device is a measure of the retention of the power conversion efficiency of the cell. Solar cells must be able to retain their efficiency for a long time to be considered commercially viable. Standard crystalline solar cells can retain their efficiency for more than 25 years. The highest conversion efficiency record for a crystalline silicon solar cell was reported to be 26.7% [2]. Hence, for a perovskite solar cell to become commercially viable, they need to demonstrate similar performances as that of their silicon counterparts. Despite the continued commercial preference for silicon solar cells, perovskite devices have gained significant attention over the years due to their remarkable properties and performance.

The power conversion efficiency (PCE) of such devices has grown rapidly from 0-2% in 1975 to a certified 25.5% recently [9]. This has been made possible due to several factors such as better selection of materials for the absorber layer, Hole Transport Layer (HTL), and Electron Transport Layer (ETL), improvements in processing techniques [10], optimization in surface design to facilitate greater photon absorption [11], and better approaches to minimize defect density such as passivation technology and encapsulation techniques [12]. A chart depicting the evolution of PCEs for several solar cell technologies is shown in Figure 1.
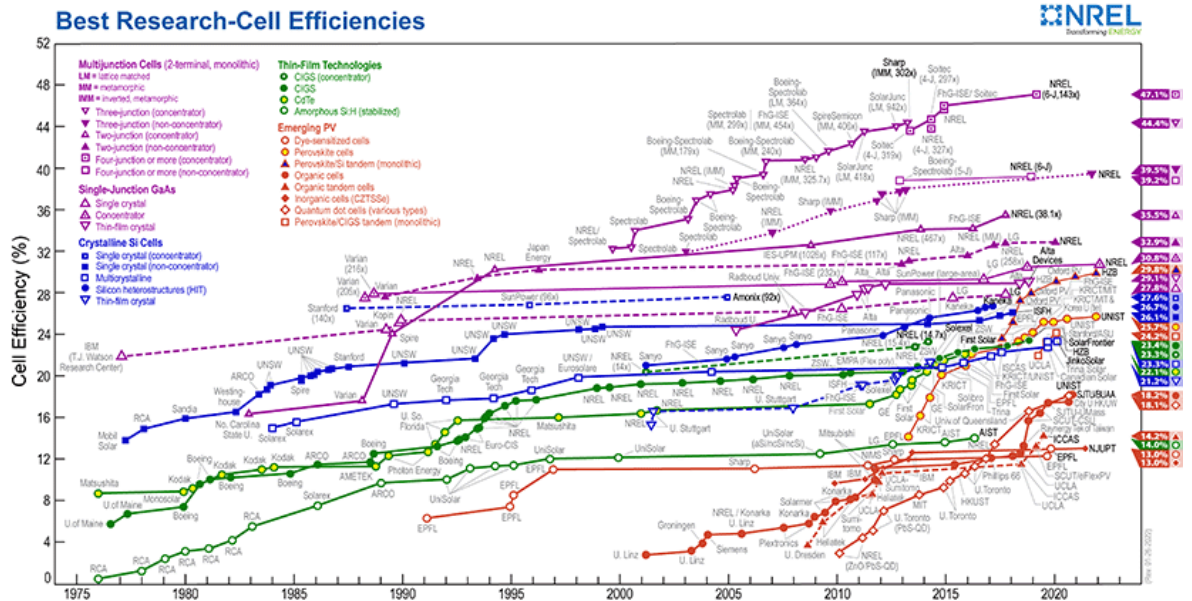
Figure 1. Chart of the highest confirmed conversion efficiencies for research cells for a range of photovoltaic technologies[13].

1.1.2 Current challenges faced by solar cells:

Over just 15 years, the record PCE of single-junction perovskite solar cells has risen from a mere 2.2% in 2006 to over 25% in 2023, a drastic improvement in the device performance that took more than 40 years for conventional silicon solar cells to achieve[9]. These tremendous improvements in device efficiencies have been made possible via bandgap engineering[14], better fabrication practices[12], incorporation of mixed halide perovskites[7], solvent engineering[15], and selection of better transport layer materials[16], to mention a few. Despite these improvements, device stability remains a central issue that prevents the long-term commercialization of perovskites. Current perovskite devices lose their efficiency over several months. This is primarily due to contamination of the perovskite film due to ambient moisture, which then promotes ion migration, disrupting the film crystallinity and affecting the performance[17]. It is important to develop better experimental practices and new methods that can improve the

3

reliability of these devices and enable their performance to arrive on par with that of conventional silicon solar cells.

1.2 Structure of the perovskite solar cell:

Perovskite solar cells have attracted extensive attention since their invention by Miyasaka and co-workers in 2009[7]. The conventional perovskite crystal structure conforms to that of a cubic crystal. Figure 2 illustrates the crystal structure of perovskite. Perovskites possess a chemical formula of ABX_3. Here, A and B are monovalent and divalent cations, respectively. A-cations are situated at the center of the unit cell while the B-cations occupy the corners of the unit cell. B is generally comprised of lead (Pb) or tin (Sn) atoms. X comprises halogen atoms, namely iodine (I), bromine (Br), or chlorine (Cl). These are located at the octahedral voids, such as the edge centers of the unit cell. These X-anions form an octahedral network around the B-cations.
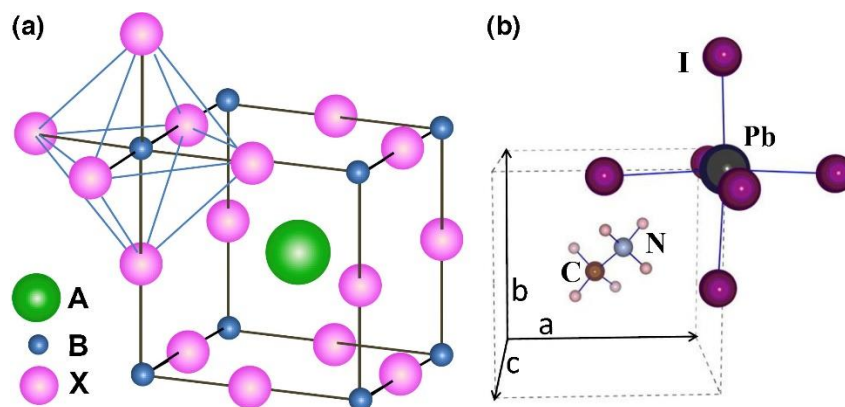
Figure 2. The perovskite crystal structure, comprising the A-site and B-site cations and X-halides; b) Unit cell of cubic $CH_3NH_3PbI_3$ perovskite[8].

1.3 Working of a perovskite solar cell:

The standard design of a perovskite solar cell is illustrated in Figure 3. A typical perovskite device comprises four thin films deposited over a conducting substrate: the Electron Transport Layer (ETL), the perovskite layer (also called the absorber layer, since this is the region that

absorbs most of the incident light intensity), the Hole Transport Layer (HTL), and metal back contacts (usually deposited via silver or gold). Solar cells wherein the ETL is deposited first comprise n-i-p device architectures (where the n, i, and p denote n-doped ETL, perovskite insulator, and p-doped HTL). Here, the incident light falls first on the n-side. A fraction of the light is absorbed by the ETL, generating electron-hole pairs, while the rest is transmitted through the cell. The perovskite layer is the region that absorbs the most out of the transmitted light. Hence, this region generates the maximum number of electron-hole pairs. These charge carriers are then separated via the built-in electric field provided by the p-n junction. The n-doped ETL provides a medium for the efficient transport of the negatively charged carriers (electrons) while the p-doped HTL provides the medium for the hole transfer. The individual charge carriers are collected at the substrate and metal contacts, respectively.
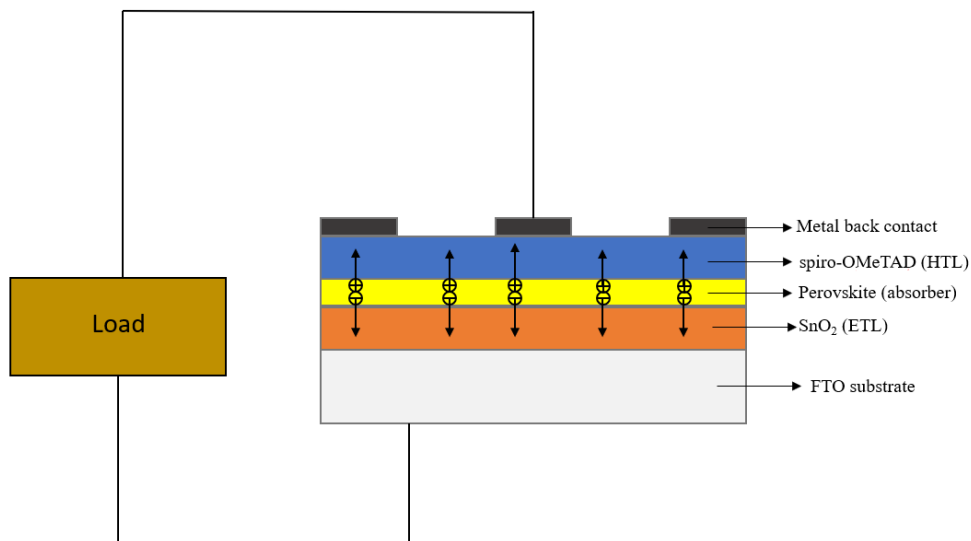
Figure 3. The standard design of a perovskite solar cell.

1.3.1 Relation between the diffusion length and the collection efficiency:

To ensure efficient collection of these charge carriers, these carriers must travel across the carrier-selective regions and reach the back contacts. The path traversed by a charge carrier before it recombines with an opposite charge carrier is called the diffusion length.

$$L = \sqrt{D\tau}$$

The diffusion length is affected by factors such as the thickness of the transport region, trap density within the region, and the number of intrinsic carriers in the region. Out of these careful attention needs to be placed on the trap density. The presence of defects such as pinholes within the film serves as trap states that effectively capture an electron or a hole. Once a charge carrier is captured, these states act as recombination centers wherein a carrier bearing an opposite charge may recombine with the captured charge carrier, leading to non-radiative recombination which is detrimental to the performance of the device. Furthermore, these trap states then serve to lower the diffusion length of the charge carriers, reducing the collection efficiency of the device. For this purpose, these transport layers are carefully fabricated to ensure a film with the least trap density and higher charge collection efficiency. Furthermore, these transport layers are also fabricated with a thickness that is comparable to the diffusion length of the charge carrier.

1.4 Key photovoltaic parameters:

Four photovoltaic parameters are of immense importance when evaluating the performance of a solar cell. These are the open-circuit voltage (V_{oc}), short-circuit current (J_{sc}), fill factor (FF), and power conversion efficiency (PCE).

The open circuit voltage is the potential difference across the solar cell at zero current. It is also a measure of the charge extraction capability of the cell. A higher open circuit voltage would be beneficial for facilitating efficient charge separation and extraction.

The short circuit current is the maximum current that can flow across the cell when the potential difference across the cell is zero. For a current to flow across the solar cell, charge carriers must be generated in the perovskite layer and then transported across the transport layers to the electrode. The potential difference generated across the solar cell creates an electric field that separates the generated charge carriers.

The fill factor (FF) of a device is the ratio of the maximum power that can be extracted from the device and the product of the short circuit current and the open circuit voltage.

$$FF = \frac{P_{mp}}{V_{OC} \times J_{SC}} = \frac{V_{mp} \times I_{mp}}{V_{OC} \times J_{SC}}$$

Here, P_{mp} is the maximum power that can be extracted from the device, and V_{mp} and I_{mp} are the potential difference and current at the maximum power, respectively.

The power conversion efficiency of the solar cell is the amount of power that is converted into usable energy from the total incident power on the cell.

$$PCE = \frac{V_{OC} \times J_{SC} \times FF}{P_{in}}$$

1.4.1 Factors affecting the device performance:

Power conversion efficiency is a critical parameter that is used to estimate the performance of a solar cell. Several factors influence the PCE of a solar cell device, such as the film crystallinity, absorption spectrum of the perovskite film, film defects, radiative/non-radiative recombination, charge separation, trap density, ambient temperature, and bandgap. Of most importance from these factors is the trap density of the film, which we will discuss further.

1.4.1.1 Presence of trap states:

The power conversion efficiency of a solar cell is indirectly influenced by the presence of trap states in the perovskite or the transport layers. Despite improvements in thin film deposition techniques, the underlying films comprising the perovskite continue to possess defects such as pinholes or vacancies. These defects lead to so-called 'trap states' which capture an electron (or a hole) and lock the charge carrier in place, preventing it from reaching the electrode. This leads to a reduction in the overall short circuit current density and consequently affects the efficiency of the device. Furthermore, as mentioned before, these trap states can serve as non-radiative recombination centers. Under non-radiative recombination, an electron and a hole combine and release energy in the form of heat. This kind of recombination is particularly undesirable in solar cells as it increases the temperature of the device which effectively lowers the open-circuit voltage of the cell, thereby negatively impacting its efficiency.

1.5 Material selections for the solar cell:

Numerous factors go into the construction of a solar cell. Some of these factors are material selection of the electron and hole transport layers, synthesis of the perovskite precursor with a desirable band gap, and choosing the appropriate deposition mechanism for each of these precursors.

When selecting the most appropriate material for the electron and hole transport layers, several criteria need to be first considered. Some of the favorable criteria amongst these include:

1.   Good energy level alignment for efficient charge transfer.

2.   High electron mobility: This will lead to fast charge transport across the ETL.

3.   High transmittance: To reduce optical energy loss.

4.   High stability: The films should not degrade under normal operating conditions

5.   Easy processing: For efficient bulk production

6.   Low cost

Based on these factors, there can be several suitable candidates for the ETL, such as organic materials like graphene, fullerene and its derivatives, or inorganic materials such as ZnO[18]. These precursors are easy to synthesize via solution processing and demonstrate high performance when used in solar cells. However, their disadvantage is their relatively short stability when exposed to the ambient environment. These materials degrade quickly over time in the presence of heat and moisture. Hence, several works have tried to use more stable alternatives such as TiO_2 and SnO_2[16,19–24]. Amongst these alternatives, Tin Oxide (SnO_2) is gaining attraction over TiO_2 as the primary electron transport layer. Tin oxide possesses high electrical conductivity and high bulk electron mobility with lower photon losses. The material can be processed easily using low-temperature methods. Finally, it demonstrates excellent chemical stability, resistance to UV radiation, and less photocatalytic activity.

1.6 Research Objective:

The primary motivation of this research was to improve the quality of the electron transport layer that goes into the fabrication of the perovskite solar cell. In this approach, we chose pure tin oxide (SnO_2) and Indium-doped tin oxide (ITO) as the electron transport layers. We used two techniques to synthesize the electron transport layer: Chemical bath deposition for the deposition of pure SnO_2 and RF sputter deposition for ITO. The process parameters for each fabrication step were isolated and modulated to determine the best process conditions that would yield high-quality films.

In the case of chemical bath deposition, the process parameters that were evaluated were, namely, the amount of the $SnCl_2$ precursor and the deposition time. In the case of chemical bath deposition, complete devices were designed after depositing the films and the power

conversion efficiencies for each of these devices were checked using a Keithley 2400 sourcemeter.

For the RF sputtering of ITO films, a ULVAC JSP 8000 sputterer was used in these experiments. In the case of the sputter-deposited films, we studied the process conditions that would produce the best film conductivity. These process conditions include the gas type (Ar, N_2, and O_2), the gas flow, and the substrate temperature. The film resistance of each of these ITO films was measured using the sourcemeter.

CHAPTER 2: DEPOSITION TECHNOLOGIES

This chapter will discuss the two deposition methodologies used for fabricating the electron transport layers and their underlying concepts.

2.1 Chemical Bath Deposition:

Chemical bath deposition (CBD) has recently emerged as a promising wet chemistry process for thin film deposition[25–27]. In this process, various precursor chemicals are mixed inside a chemical bath which is heated to sufficiently high temperatures. The elevated deposition temperature accelerates the rate of reaction between the precursor chemicals and assists in the formation of a thin film over the substrate. The reaction proceeds via heterogeneous nucleation of the film over the surface of the substrate.

Conventional methods of fabricating the electron transport layer in perovskite solar cells include spin coating, thermal evaporation, or sputtering. However, several of these methods damage the ETL. The primary damage to the ETL stems from the presence of pinholes in the film, which act as non-radiative recombination centres for charge carriers, leading to reduced open circuit voltage, reduced short circuit current, and reduced fill factors. Furthermore, defects at the perovskite/ETL interface, which may be attributed to lattice mismatch between the perovskite and the ETL, can also act as non-radiative recombination centers and effectively promote charge capture, thereby hindering the charge extraction efficiency. Improper band alignment between the perovskite and the ETL can also lead to bad electron extraction and bad hole blockage. This leads to worse charge separation and contributes to reduced performance in perovskite solar cells. To address these issues, Chemical Bath Deposition was introduced as a unique and facile method to assist the deposition of electron transport layers in a way that achieves good film uniformity via an inexpensive process.

Although little is known regarding the mechanism of chemical bath deposition, a few authors such as Yoo et al have suggested one possible mechanism of the process[27]. The presence of acidic media in the solution (in this case, HCl) controls the solubility of the $SnCl_2$ in the solution. The common ion effect on the solubility of the $SnCl_2$ would prevent complete dissociation of the chemical into the solution so that the initial precursor in the solution would still be $SnCl_2$. When urea is added to the solution, it reacts with water to form ammonium carbonate which quickly undergoes decomposition to form ammonia, carbon dioxide, and water. The presence of ammonia slightly increases the pH of the solution. Furthermore, the presence of additional water molecules increases the amount of hydroxide ions in the solution. The Sn^{2+} ions react with these hydroxide ions to form $Sn(OH)_4$ which then dissociate to form SnO_2 and water. However, since there now is a deficiency of hydroxide ions in the solution, further oxidation of Sn^{2+} to Sn^{4+} is stopped, making the oxidation of Sn^{2+} ions incomplete. These remaining Sn^{2+} ions enter into the lattice of SnO_2 owing to the comparable ionic radii between the two ions (0.62 Å for Sn^{2+} and 0.69 Å for Sn^{4+}). This forms an incomplete compound of SnO_{2-x}. This is indicated by a slight murkiness in the solution. Other compounds such as SnO and $Sn_6O_4(OH)_4$, are also formed as a result of this oxygen-deficient solution.
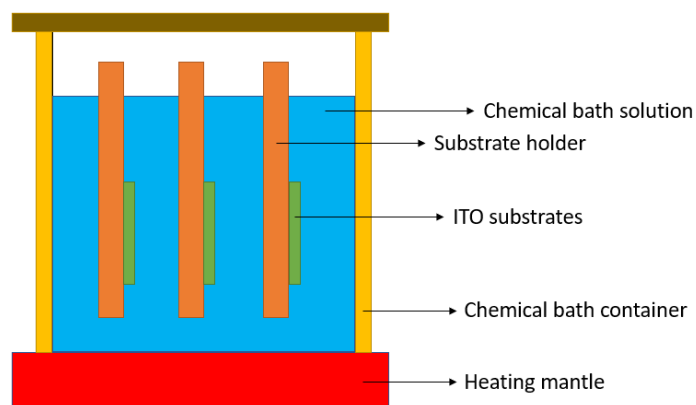
Figure 4. Schematic of the Chemical Bath Deposition setup.

2.2 RF Sputtering

Sputtering refers to the removal of ions/atoms from the surface of a solid when energetic ions hit the surface[28,29]. The energy and momentum of the incident ions get transferred to the surface atoms which cause them to be ejected from the solid. These ejected ions are deposited on the substrate and form the thin film. Hence, sputtering is also known as sputter etching and can be viewed as the process of erosion of the target surface by the energetic incident ions.

There are two ways of bombarding the energetic ions on the target and correspondingly there are two cases of ion beam sputtering and plasma sputtering. In ion beam sputtering, an ion-beam source of noble gases is placed inside the vacuum chamber which is deferentially pumped. Ions from the source are directed toward the target surface and cause sputtering. In the second method of plasma sputtering, the chamber is filled with noble gas, also called working gas at low pressure. A glow discharge (DC or RF) is produced between two electrodes. The target acts as the cathode and the substrate and/or the chamber walls act as the anode. In the glow discharge, the charged ions of the working gas are accelerated so that they gain enough energy to cause sputtering. For sputtering, the incident ions should have energies of the order of a few hundred electron volts.
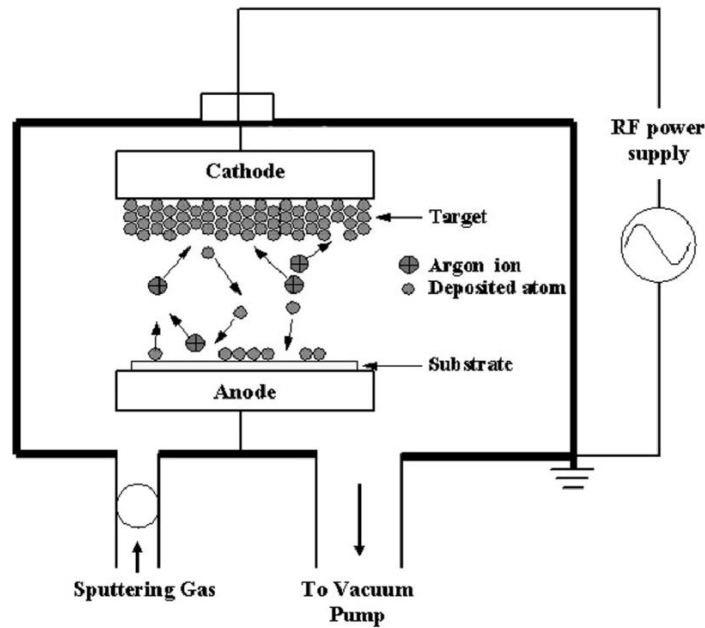
Figure 5. Schematic of the RF sputter deposition setup[30].

The RF sputtering system utilizes a high-frequency power supply to generate the plasma plume. In this plasma plume, the ions possess greater inertia than the electrons on account of their bigger mass. Hence, when the RF power is applied, they fail to move as fast as the electrons can in the rapidly changing applied field. Thus, the current through the electrode will be unequal. To make this current equal, a DC self-bias is developed on the electrode. This DC self-bias is negative with respect to the plasma potential and reduces the current due to electrons in such a way that the current due to electrons and ions are equal. As the heavy ions largely respond to this DC self-bias, the ions are accelerated toward the target and cause sputtering. Hence, the DC self-bias is the potential difference between the RF electrode (target) and the plasma plume generated between the substrate and the target. The greater the magnitude of the DC bias, the greater will be the acceleration of the ions toward the target. Once these accelerating gaseous ions sputter the target particles, they transfer their momentum to the sputtering particles. As a result, the speed of the target particles towards the substrate will be greater for higher magnitudes of RF power. If the momentum of these sputtered particles upon

14

contact with the substrate is greater at these higher RF power magnitudes, then these particles would travel deeper into the substrate material and possibly damage the perovskite film in the process. However, if the momentum of these particles is too low, then these particles may lose their momentum upon collisions with the working gas or the chamber particles before they arrive at the substrate surface. Hence, it is necessary to properly tune the RF power to obtain the optimum power at which these target particles would deposit on the substrate without damaging the underlying perovskite film. An understanding of the relationship between RF power and the DC self-bias would facilitate this objective.

CHAPTER 3: METHODOLOGIES

In this chapter, the various experimental methodologies are discussed: Preparation of the ETL via chemical bath deposition, preparation of the perovskite layer, preparation of the HTL, and preparation of the ITO via sputtering.

3.1 Preparation of the SnO$_2$ Electron Transport Layer via Chemical Bath Deposition

The temperature conditions for the preparation of the chemical bath were taken at a room temperature of 22.3°C and a relative humidity of 47.1%. To prepare the solution for the chemical bath, 40 mL of deionized water was taken in which 0.5 mL of HCl, 10 µL of TGA, 110 mg of SnCl$_2$, and 0.5 g of urea were mixed with constant stirring.

The substrates were first prepared via sequential washing with detergent, deionized water, acetone, and isopropanol in an ultrasonicator. Following this, the substrates were blow-dried using an N$_2$ gun and subjected to UV-Ozone treatment for 30 minutes. Treating the substrates with UV-Ozone eliminates surface impurities, reduces oxygen vacancies, and improves the wettability of the film. The substrates were then taped onto substrate holders using Kapton tape and then immersed into the chemical bath.

3.2 Preparation of the perovskite layer:

In our experiments, we used a mixed halide perovskite MA$_{0.05}$FA$_{0.95}$PbI$_3$. For mixed halide perovskites, composition engineering is carried out to achieve the optimum MA/FA ratio that would yield a desirable band gap. A composition ratio of 95% FAPbI$_3$ and 5% MAPbI$_3$ was found to be ideal for our experiments.

The perovskite solution is a mixed halide solution comprising 95% FAPbI$_3$ and 5% MAPbI$_3$. This was prepared by mixing four chemical constituents which are 0.8 M solutions each of

MAPbBr$_3$, MACl, PbI$_2$, and FAI in a DMF-DMSO solution of a volume ratio of 8:1. This solution is then sent through a 0.2 μm filter.

The deposition of the perovskite solution over the SnO$_2$-deposited substrates is carried out in a controlled atmosphere, inside a nitrogen-filled glovebox. The deposition takes place via the process of spin coating. First, we ensure that the pressure inside the glovebox is kept at a constant of 30 psi. with an oxygen amount of less than 2 pm. The SnO$_2$-deposited substrates are placed inside the glovebox. A 40 μL perovskite solution is spin-coated over these substrates. After this deposition, the substrates are allowed to spin at 3,000 rpm for 30 seconds. A small amount of 600 μL of Diethyl Ether is also spin-coated over the perovskite film. Diethyl ether acts as an antisolvent by reducing the solubility of the solution and inducing the precipitation of the perovskite from the solution. Following this, the film is taken out and placed on a heating mantle at 60°C. until it turns black. Heating the perovskite film at 60°C induces a phase transformation from the α-phase to the δ-phase. The perovskite changing color from yellow to black indicates a change in phase from α-phase to δ-phase. After the film has turned completely black, the film is transferred to another heating mantle kept at 150°C. This completes the transformation to the δ-phase and also evaporates any remaining MACl in the film.

3.3 Preparation of the Hole Transport Layer:

Before depositing the hole transport layer, a passivation layer is first deposited over the perovskite layer. This passivating material serves as a barrier to prevent moisture and other foreign elements from entering the perovskite layer. In the process, it prevents any damage to the perovskite film. In addition, it acts as a passivation layer to reduce the recombination at the perovskite-HTL interface. In our experiments, we use n-octylammonium iodide (OAI) as the passivation layer. 25 μL of OAI is pipetted out and spin-coated over the perovskite layer at a rotation speed of 4,000 rpm for 30 seconds. Initially, the perovskite film is allowed to spin on

the spin coater. After about 15 seconds, the OAI is deposited onto the film. After the deposition is complete, the film containing OAI is transferred onto a heating mantle kept at 100°C. The film is left to dry for 10 minutes.

The Hole Transport Layer chosen for our experiments is a solution of spiro-OMeTAD (2,2',7,7'-tetrakis(N,N-di-p-methoxyphenylamine)-9,9'-spirobifluorene). 25 μL of spiro-OMeTAD is spin-coated onto the film under a rotation speed of 3,000 rpm. The film is allowed to spin for 30 seconds after which it is transferred into a vacuum antechamber and left overnight.

3.4 Preparation of ITO via sputtering

The sputtering process was performed in the Integrated Systems Nanofabrication Cleanroom located at the California NanoSystems Institute at UCLA. The substrates are taped onto a substrate holder using Kapton tape and loaded into the chamber. The process recipes for the sputter deposition are created and the recipes are run. The various process parameters that are used are Gas type (Ar, N_2, O_2), gas flow, substrate temperature, RF power, and sputtering time.

CHAPTER 4: RESULTS AND DISCUSSION

4.1 Results on the Chemical Bath Deposition of SnO$_2$:

High-purity SnO$_2$ was deposited over ITO substrates via chemical bath deposition using different amounts of SnCl$_2$ at different deposition times. The results are summarized below.

Chemical baths containing different amounts of SnCl$_2$ were prepared. The substrates were immersed in the chemical baths for different deposition times. Table 1 and Table 2 provide simple designation frameworks for each of the different SnCl$_2$ amounts and deposition times. Table 3 comprises a list of the device designation for each device subjected to a specific process condition.

Amount of SnCl$_2$	Designation
70 mg	C1
90 mg	C2
110 mg	C3
130 mg	C4
150 mg	C5

Table 1. Designations for the chemical baths containing different amounts of SnCl$_2$.

Deposition time (hrs)	Designation
3.5	T1
4	T2
4.5	T3

Table 2. Designations for the different deposition times during fabrication.

As can be seen in the table above, the individual amounts of $SnCl_2$ chosen are designated by C1-C5 and the deposition times are designated by T1-T3. The compiled information showing the different device designations for each condition is given in Table 3.

Amount of SnCl₂ (mg)	Deposition time (hrs)	Device Designation
70	3.5	C1T1
70	4	C1T2
70	4.5	C1T3
90	3.5	C2T1
90	4	C2T2
90	4.5	C2T3
110	3.5	C3T1
110	4	C3T2
110	4.5	C3T3
130	4	C4T2
150	4	C5T2

Table 3. Device designations for each of the process conditions.

4.1.1 Time-independent IV curves:

Figure 6 shows the IV curves for the C1-C5 devices at a deposition time of 4 hours. From this, it can be seen that the best electrical performance is demonstrated by the C4 device. One can the superior open circuit voltage, short circuit current, and fill factor for this device.
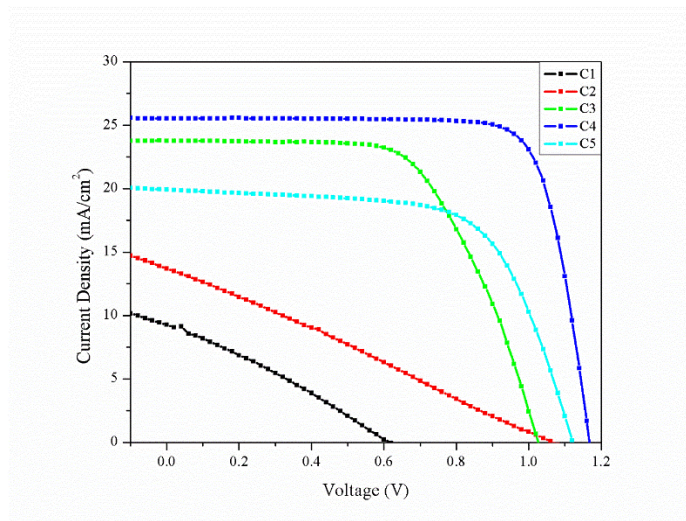

Figure 6. IV curves for devices C1-C5 at 4 h deposition time.

4.1.2 Variation of the photovoltaic parameters with the precursor amount:

The corresponding Figure 7 shows the variation of the Power Conversion Efficiency with the amount of $SnCl_2$ at a deposition time of 4 hours. We see an increasing trend in the PCE of these devices, a marked increase upto 130 mg $SnCl_2$ following which the PCE drops slightly. Undoubtedly, the best PCE is exhibited by the device fabricated using 130 mg of $SnCl_2$. The champion PCE exhibited for this set of devices was 23.80% at an $SnCl_2$ amount of 130 mg at a deposition time of 4 hours. These high PCE values at greater $SnCl_2$ amounts can be attributed to better coverage of the substrate surface with the SnO_2 films with increasing amounts of the $SnCl_2$ precursor. The drop in the PCE at C5 may be attributed to the incomplete oxidation of the Sn^{2+} ions in the solution. As mentioned before, these unoxidized Sn^{2+} ions intercalate into the SnO_2 lattices and affect the band alignment of the film. The formation of these SnO_{2-x}

21

particles indicates a greater number of oxygen vacancies in the lattice, which may act as non-radiative recombination centers and effectively capture transporting electrons.
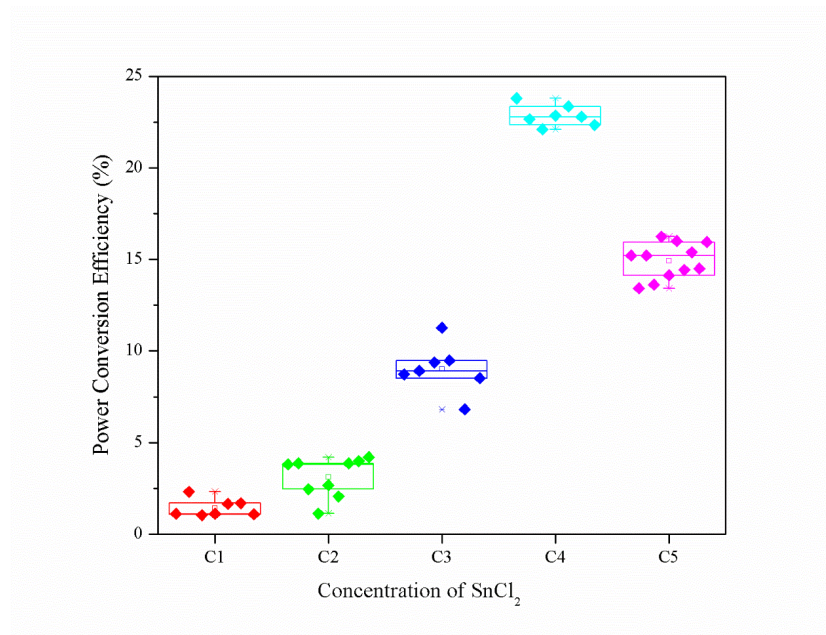
Figure 7. Variation of the power conversion efficiency with the amount of $SnCl_2$ at a deposition time of 4 hours.

Figure 8 shows the variation of the short circuit current with the precursor amount. We can observe the much lower short circuit current from device C5 as a result of the increase in electron capture via the non-radiative recombination centers generated due to the oxygen vacancies created by the partially oxidized Sn^{2+} ions.
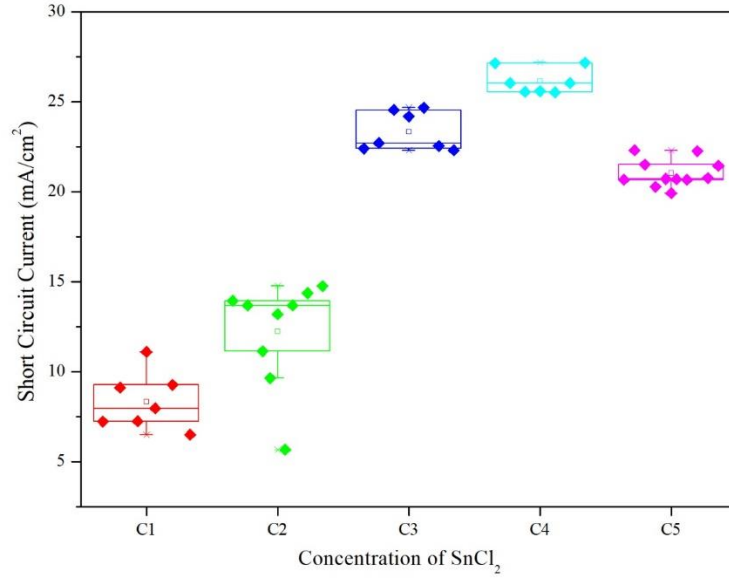
Figure 8. Relationship between the short circuit current and the SnCl₂ amount at a deposition time of 4 hours.

The behavior of the open circuit voltage with the precursor amount is shown in Figure 9. Notably, the open-circuit voltage (Voc) is not so much affected for the C5 device. The open circuit voltage has a logarithmic dependence with the short circuit current according to the following equation:

$$Voc = \frac{kT}{q}\ln\left(\frac{Jsc}{Jo} + 1\right)$$

Hence, a large increase in the short-circuit current would have little effect on the open-circuit voltage. Although the open-circuit voltage is influenced by the increase in the number of non-radiative recombination centers in the devices, its influence is minimal compared to the effect on the short-circuit current.

Figure 9. Relationship between the open circuit voltage and the SnCl₂ amount at a deposition time of 4 hours.

Considering the fill factors of each of the individual devices, the trend is as expected, with the fill factor increasing with increasing amount and the highest fill factor exhibited for the device C4T3. This is shown in Figure 10
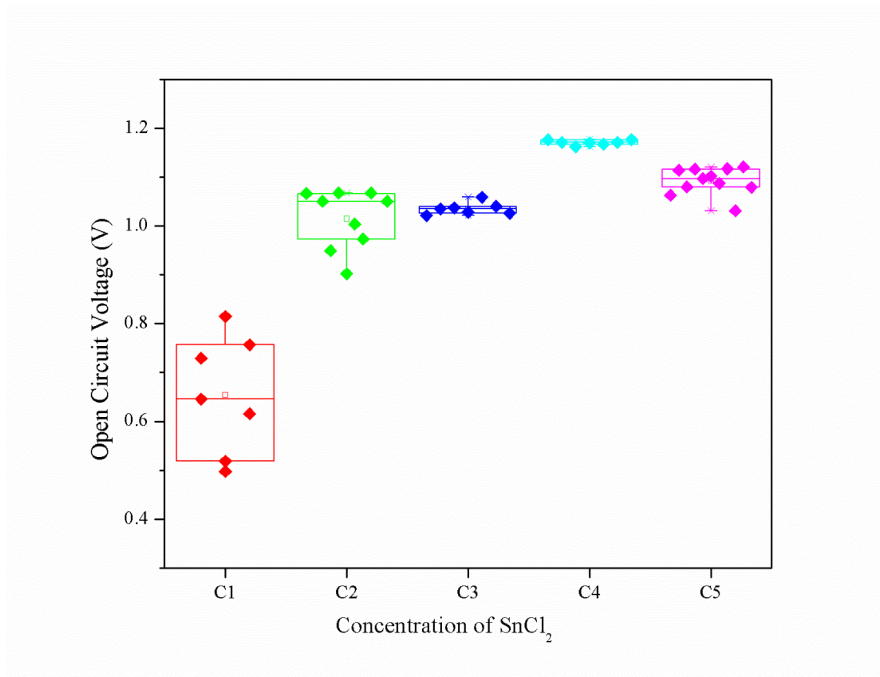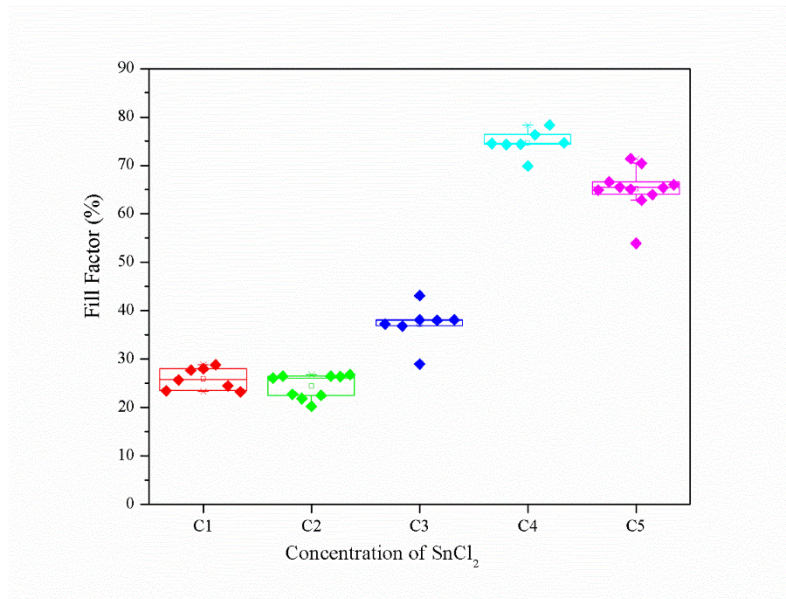
Figure 10. Relationship between the Fill Factor and the SnCl₂ amount at a deposition time of 4 hours.

Table 4 provides us with a complete quantitative estimation of the average values of each of the photovoltaic parameters for each device. It can be seen that the best efficiency was recorded for the device C4T2, fabricated using 110 mg $SnCl_2$ at a deposition time of 4 hours.

Device	Open Circuit Voltage (V)	Short Circuit Current (mA/cm^2)	Fill Factor (%)	PCE (%)
C1T2	0.65	8.35	25.92	1.43
C2T2	1.01	12.24	24.38	3.12
C3T2	1.04	23.34	37.21	9.02
C4T2	1.17	26.15	74.64	22.84
C5T2	1.09	21.02	65.10	14.92

Table 4. Average V_{oc}, J_{sc}, FF, and PCEs of each device at a deposition time of 4 hours

4.1.3   Variation of the photovoltaic parameters with the deposition time:

The following figures show the effect of each of the photovoltaic parameters with the deposition time for each amount of the $SnCl_2$ precursor. All three parameters: Jsc, Voc, and FF for the C1 and C2 devices are observed to increase with the deposition time, leading to an overall increase in the PCE. As mentioned before, this would be due to the increasing coverage of the film over the substrate. No significant relation in any of the photovoltaic parameters was observed in the C3 devices.
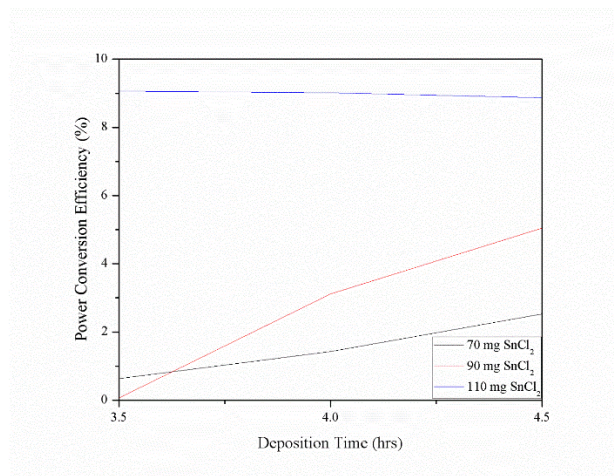
Figure 11. PCE variations with deposition time for different SnCl₂ amounts.
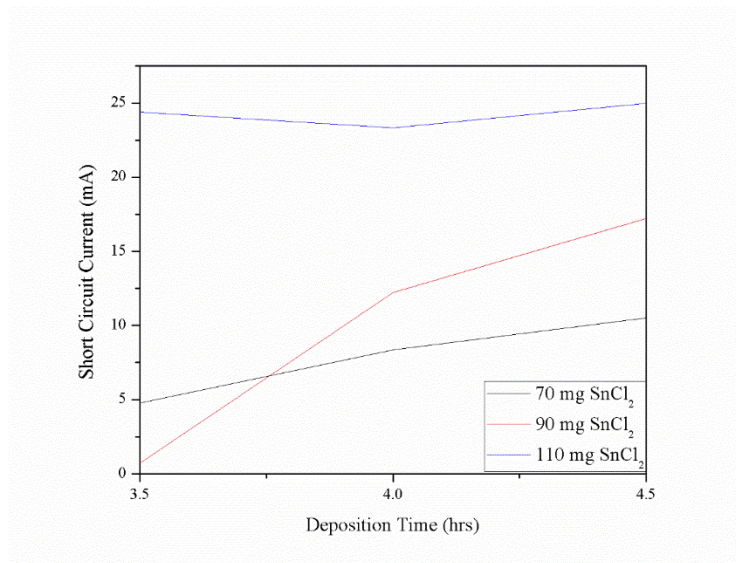
Figure 12. Short circuit current variations with deposition time for different SnCl₂ amounts.
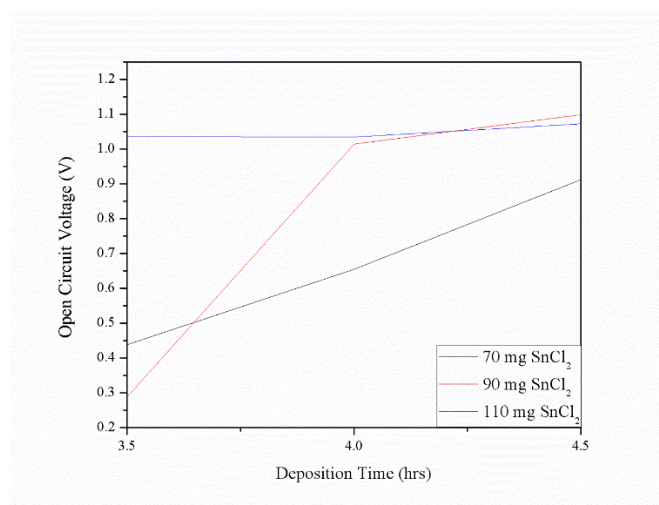
Figure 13. Open circuit voltage variations with deposition time for different SnCl₂ amounts.
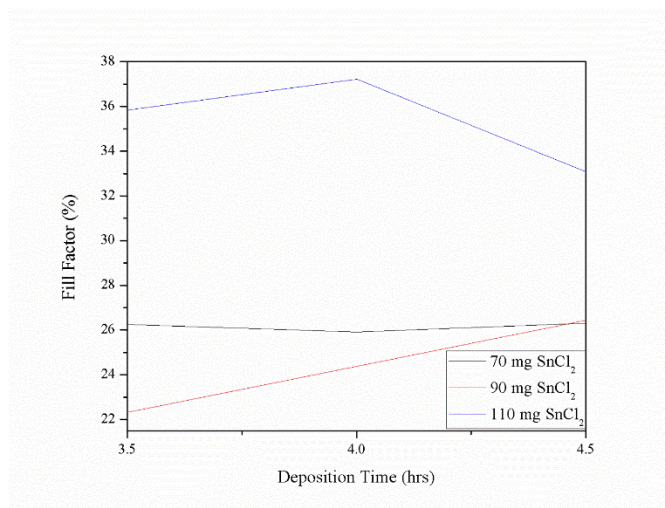
Figure 14. Fill factor variations with deposition time for different SnCl$_2$ amounts.

The quantitative average values of the photovoltaic parameters for all the other devices are displayed in Table 5, Table 6, and Table 7.

Device	Open Circuit Voltage (V)	Short Circuit Current (mA/cm^2)	Fill Factor (%)	PCE (%)
C1T1	0.44	4.76	26.25	0.63
C1T2	0.65	8.35	25.92	1.43
C1T3	0.91	10.52	26.31	2.53

Table 5. Average Voc, Jsc, FF, and PCEs of each device at an SnCl$_2$ amount of 70 mg.

28

Device	Open Circuit Voltage (V)	Short Circuit Current (mA/cm2)	Fill Factor (%)	PCE (%)
C2T1	0.29	0.70	22.32	0.07
C2T2	1.01	12.24	24.38	3.12
C2T3	1.10	17.21	26.43	5.04

Table 6. Average V_{oc}, J_{sc}, FF, and PCEs of each device at an SnCl$_2$ amount of 90 mg.

Device	Open Circuit Voltage (V)	Short Circuit Current (mA/cm2)	Fill Factor (%)	PCE (%)
C3T1	1.04	24.40	35.84	9.06
C3T2	1.04	23.34	37.21	9.02
C3T3	1.07	24.98	33.09	8.87

Table 7. Average V_{oc}, J_{sc}, FF, and PCEs of each device at an SnCl$_2$ amount of 110 mg.

4.2 Results on the RF sputtering of ITO:

In this set of experiments, we tried to fabricate the electron transport layers for perovskite solar cells via RF sputtering. The objective here was twofold: to understand the relationship between the RF power and DC bias, to tune the process parameters of the RF sputtering system, and determine the ideal process controls that would yield a film of good conductivity. To do this, various parameters of the sputtering system were taken into consideration, including the RF power, substrate temperature, gas type (comprising three gases: Ar, N_2, and O_2), gas flow, and sputtering time.

4.2.1 Understanding the Relationship between RF Power and DC Self-bias:

When understanding the relationship between the DC bias voltage and the RF power, it is important to closely monitor the surrounding conditions of the sputter chamber and keep them constant. Since the amount of charged gaseous ions comprising the plasma plume also determines the bias voltage, the gas flow inside the chamber was kept constant at 10 sccm of Argon. Correspondingly, the chamber pressure was also closely monitored and kept constant at 8.9×10^{-4} Torr.

The DC bias voltage at different magnitudes of RF power was measured and the behavior is depicted in Figure 15. After the appropriate curve fitting, it was found that the bias voltage has a logarithmic dependence with the RF power.

$$V_{DC} = 32.06 \ln(19.01 + P_{RF}) - 76.25$$

Using this corresponding generated equation, one can manually input the RF power value and obtain the corresponding self-bias value for the given set of process conditions (10 sccm Ar gas flow). Hence, with the above equation, the user can estimate the self-bias voltage that would be generated for a particular RF power. They would be able to exert an additional layer of control over their experimental processes.

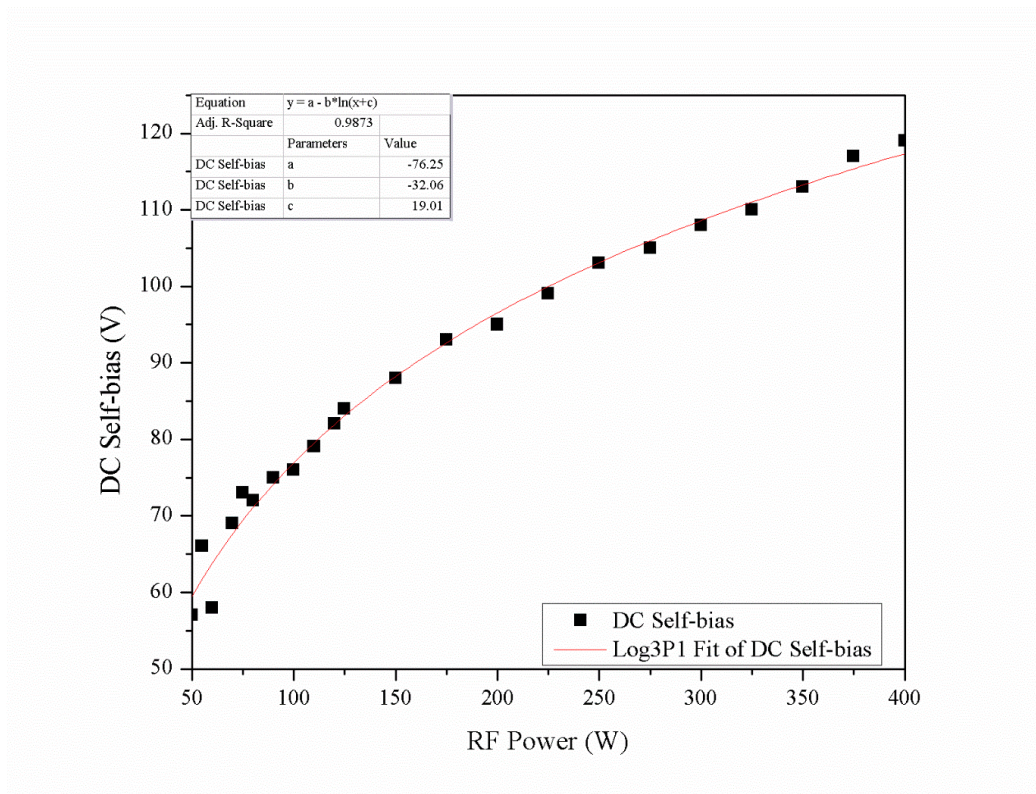| Equation	y = a - b*ln(x+c)	
Adj. R-Square	0.9873	
	Parameters	Value
DC Self-bias	a	-76.25
DC Self-bias	b	-32.06
DC Self-bias	c	19.01

Figure 15. Relationship between the RF power and DC self-bias at an Ar gas flow of 10 sccm.

4.2.2   Influence of Gas Flow on the Conductivity of ITO:

4.2.2.1 Influence of N$_2$ gas flow:

Here, the volume gas flow of the Nitrogen gas was modulated from 0 to 20 sccm while other parameters remained constant. The RF power was chosen to be 300 W with a sputtering time of 90 seconds to ensure the fabrication of a thin film of a few nanometers. The Argon gas flow was kept at 10 sccm throughout the process and no Oxygen was used. The substrate temperature was kept at room temperature.

Initially, the sputtering process was carried out in two steps: Firstly, the RF power was kept to 50 W for a sputtering time of 10 minutes to generate a thin film. Then, the RF power was raised to 200 W for a sputtering time of 8 minutes to generate a thicker film. For each batch of substrates, the nitrogen gas flow was raised from 5 sccm to 20 sccm in 2.5 sccm increments. It was found that with the increase in the N$_2$ gas flow, the mean resistance of the ITO increases linearly. This is shown in Figure 16.
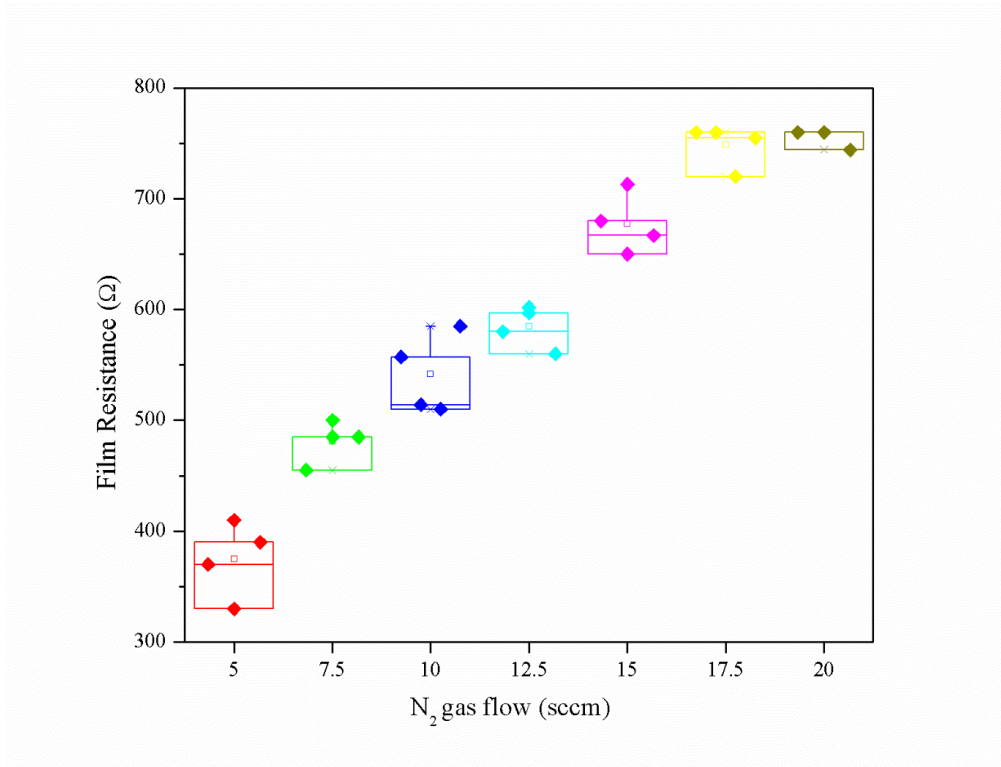
Figure 16. Relationship between N2 gas flow and film resistance at higher N_2 gas flow values.

A more detailed depiction of the individual resistance values is shown in Table 8

Ar gas flow (sccm)	O₂ gas flow (sccm)	N₂ Gas Flow (sccm)	Film Resistance (Ω)
10	0	5	375
10	0	7.5	481.25
10	0	10	541.5
10	0	12.5	584.75
10	0	15	677.5
10	0	17.5	748.75
10	0	20	853.5

Table 8. Quantified film resistance values at different N2 gas flow rates.

In the next set of experiments, the nitrogen gas flow was reduced to below 5 sccm to check for

the electrical behavior of the subsequent films. Here, we employed a one-step deposition

process and kept the RF power at 300 W for a sputtering time of 90 seconds. The N_2 gas flow was gradually reduced from 5 sccm to 0 sccm. As can be observed in Figure 17, the optimum nitrogen gas flow for the highest conductivity of the ITO films is at 1.0 sccm, following which the film resistance rises.
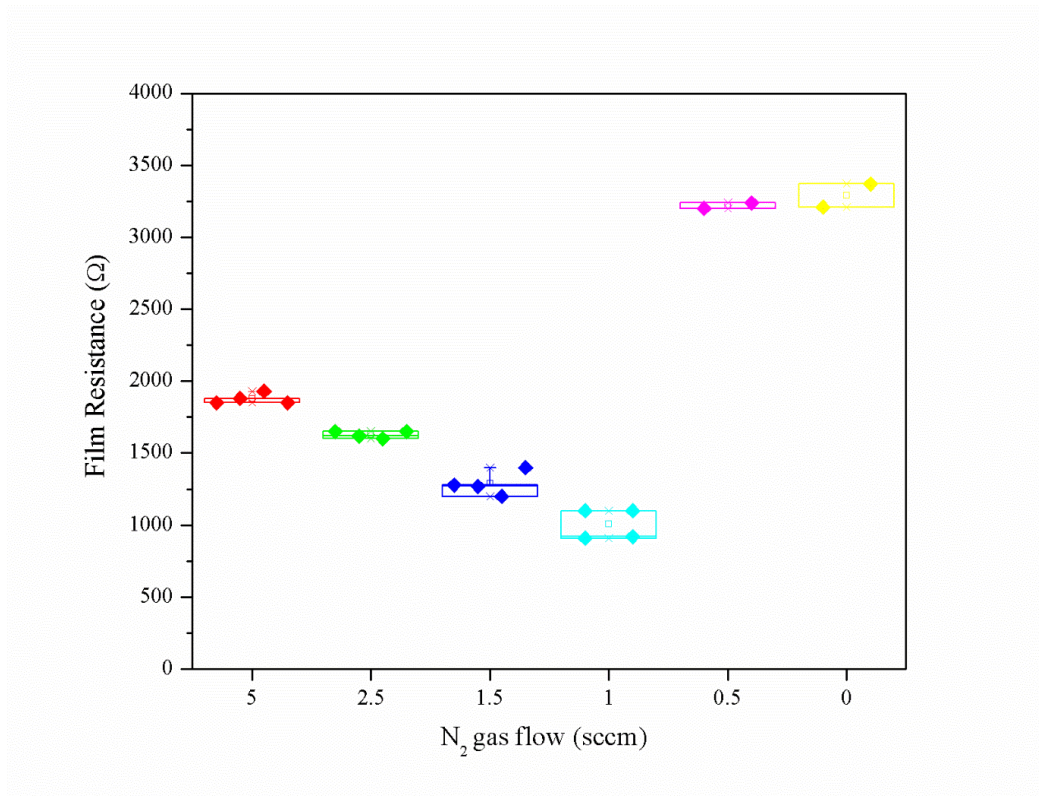
Figure 17. Relationship between N_2 gas flow and film resistance at lower N_2 values.

The following Table 9 gives the individual resistance values.

Ar gas flow (sccm)	O₂ gas flow (sccm)	N₂ Gas Flow (sccm)	Film Resistance (Ω)
10	0	5	1,877.5
10	0	2.5	1,630
10	0	1.5	1,287.5
10	0	1	1,007.5
10	0	0.5	4,722.5
10	0	0	5,335

Table 9. Quantified film resistance values at different N_2 gas flow rates.

4.2.2.2 Influence of O2 gas flow:

The influence of oxygen on the film conductivity was also studied. The data is shown in Figure 18 Here, the N_2 gas flow was kept at zero with the standard Ar gas flow at 10 sccm. From the figure, it can be seen that the best film resistivity was captured at an O_2 gas flow of 0.5. Further increase in the oxygen gas flow elevates the film resistance.

Figure 18. Relationship between O$_2$ gas flow and film resistance.

Ar gas flow (sccm)	N$_2$ gas flow (sccm)	O$_2$ Gas flow (sccm)	Film Resistance (Ω)
10	0	0	3,507.5
10	0	0.5	974.5
10	0	1	4,850
10	0	1.5	11,950

Table 10. Quantified film resistance values at different O$_2$ gas flow rates.

4.2.2.3 Influence of Ar gas flow:

Increasing the gas flow of argon atoms inside the sputtering chamber leads to ITO films with improved conductivities (Figure 19). This can result from better coverage of the glass substrate as a greater number of ITO particles would be sputtered off from the target by the increased number of Ar atoms. However, we did not bother to try increasing the Ar flow further than 30 sccm since the change in the resistance was not so pronounced after 30 sccm gas flow.
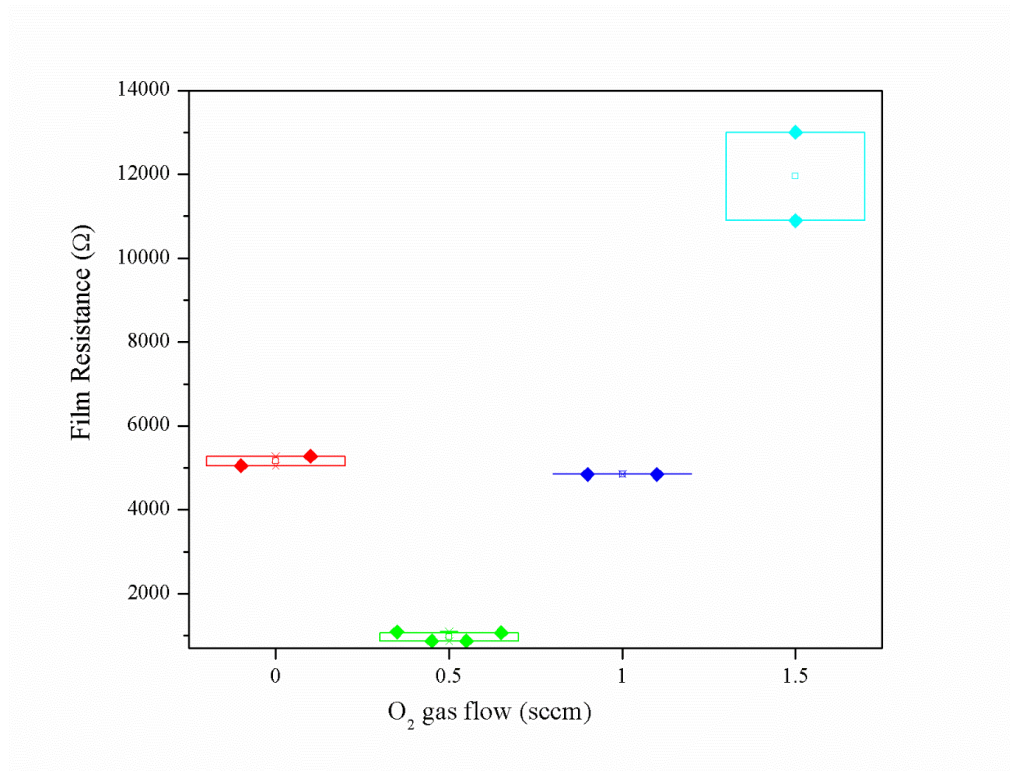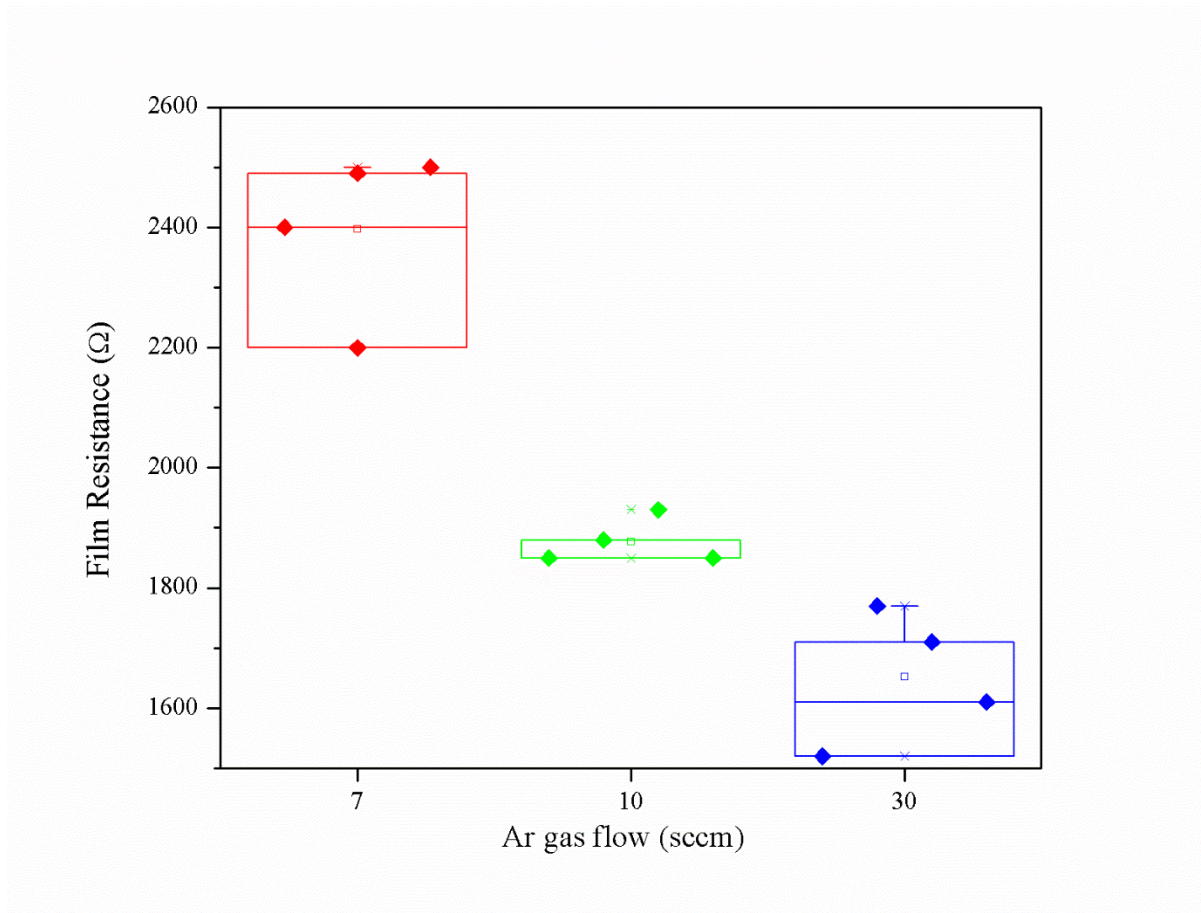

Figure 19. Relationship between Ar gas flow and film resistance.

O₂ gas flow (sccm)	N₂ gas flow (sccm)	Ar Gas Flow (sccm)	Film Resistance (Ω)
0	5	7	2,397.5
0	5	10	1,877.5
0	5	30	1,652.5

Table 11. Quantified film resistance values at different Ar gas flow rates.

4.2.2.4 Influence of Temperature on the electronic properties of ITO Films:

Here, we tried to observe the effect of temperature on the electronic properties of ITO films. The experiment was conducted in two batches. For the first batch, the temperature for each set of substrates was increased in 10-degree increments from 10ºC to 60ºC. No noticeable difference in the resistivity values was observed, as shown in Figure 20.

Figure 20. Relationship between the substrate temperature and film resistance.

38

O₂ Gas Flow (sccm)	Ar Gas Flow (sccm)	N₂ Gas Flow (sccm)	Substrate Temperature (°C)	Film Resistance (Ω)
0	10	1	10	1,310
0	10	1	20	1,490
0	10	1	30	1,490
0	10	1	40	1,210
0	10	1	50	1,500
0	10	1	60	1,470

Table 12. Quantified film resistance values at different substrate temperatures.

For the second batch, the temperatures were increased in 50-degree increments from $0°C$ to $150°C$. Here, the resistivity values remained mostly constant from a temperature sweep from $0°C$ to $100°C$, as shown in Figure 21. However, at a temperature of $150°C$, the resistivity dropped sharply by around 36%. This indicates that higher temperature regimes would yield ITO films of higher conductivity.
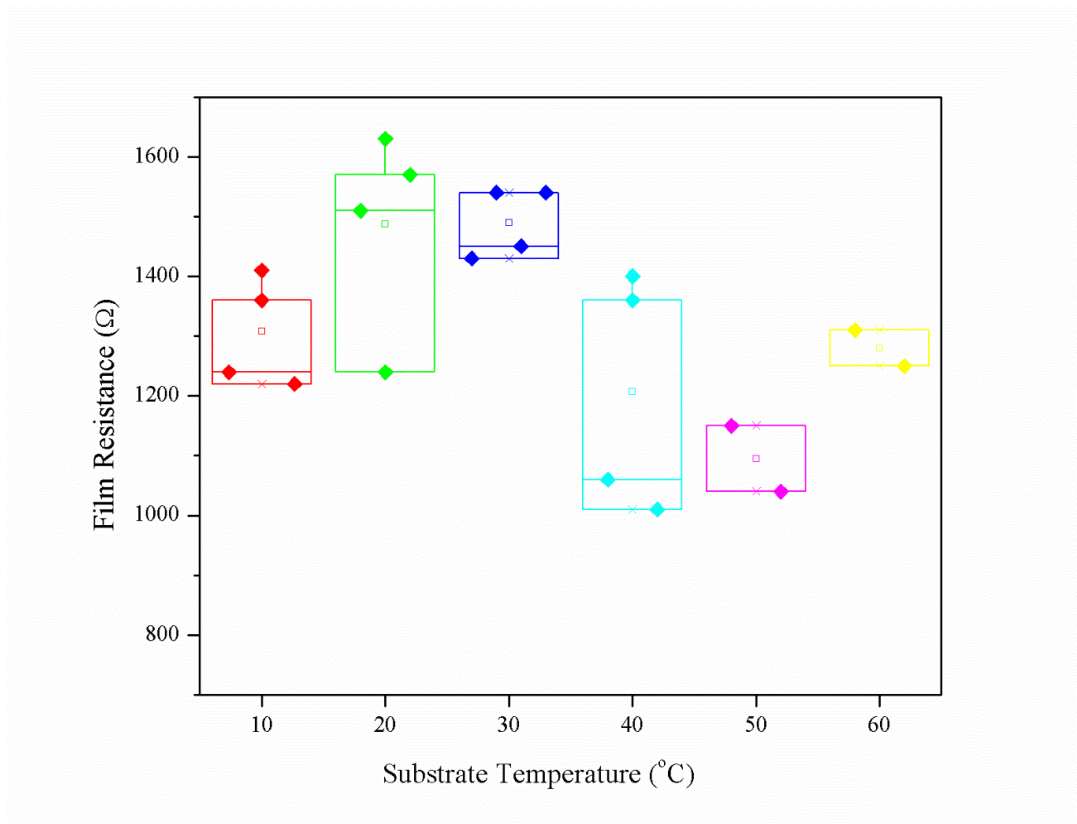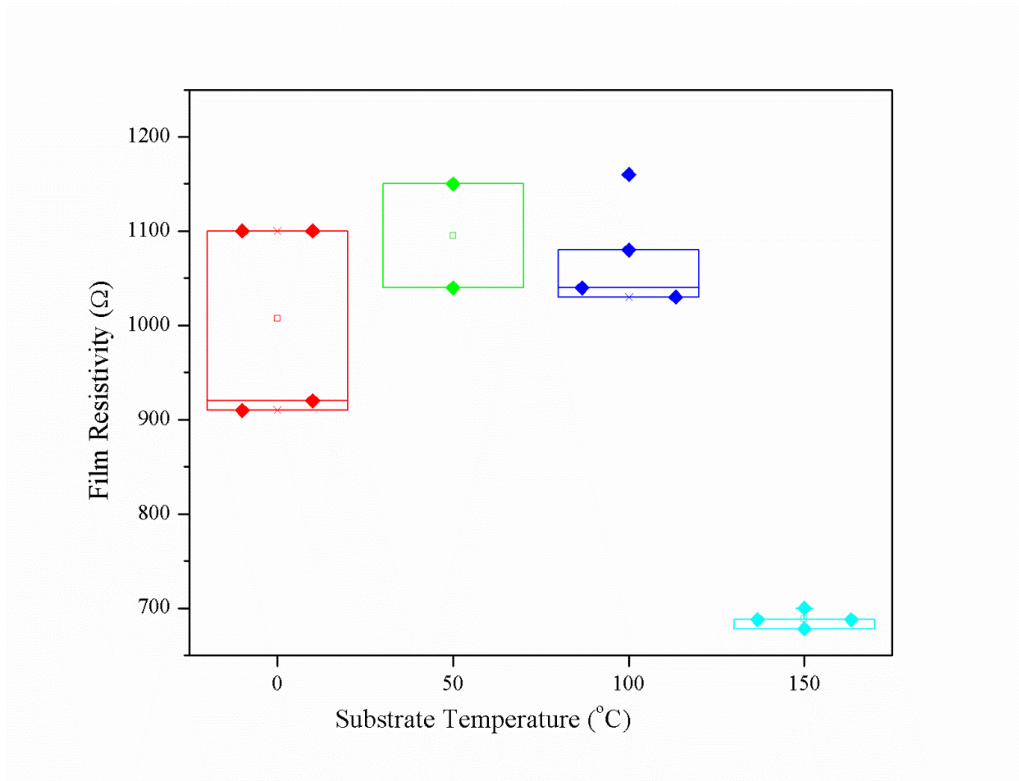
Figure 21. Relationship between the substrate temperature and film resistance.

O$_2$ gas flow (sccm)	Ar Gas Flow (sccm)	N$_2$ Gas Flow (sccm)	Substrate Temperature (ºC)	Film Resistance (Ω)
0	10	1	0	1,007.5
0	10	1	50	1,099.5
0	10	1	100	1,077.5
0	10	1	150	688.5

Table 13. Quantified film resistance values at different substrate temperatures.

Based on these results, we conclude that the deposition of high-conductivity ITO films would be carried out using an N$_2$ gas flow of 1 sccm without any O$_2$ flow. Carrying out the deposition at elevated temperatures and high Ar gas flows increases the conductivity of the films.

CHAPTER 5: CONCLUSIONS AND FUTURE WORK

5.1 Conclusions:

In this work, we fabricated the electron-selective films for lead halide perovskite solar cells using ITO via two methods: Chemical bath deposition and sputter deposition. For the chemical bath deposition experiments, we fabricated different ETLs at different amounts of the $SnCl_2$ precursor and deposition time and evaluated the device performance for each condition. The champion device efficiency was found to be 23.8% for the perovskite solar cell synthesized using 130 mg $SnCl_2$ and a 4-hour deposition time. This gives us the ideal conditions of the chemical bath that would yield devices with the best efficiencies. In the sputter deposition experiments, we fabricated different ETLs by modulating the different sputter parameters such as gas type, gas flow rate, and temperature. In the process, we obtained the ideal process parameters that would yield the best-performing ITO. The sputter deposition process should essentially be carried out using 1 sccm N_2 and 30 sccm Ar with no oxygen flow. Carrying out the deposition process at elevated temperatures results in a better conductive film. These sets of experiments demonstrate that, by acquiring greater process control over the deposition of ITO thin films during the fabrication of perovskite solar cells, one can improve the overall device performance.

5.2 Future work:

The current experiments determine the optimum process conditions that would yield a high-quality electron transport layer for high-performing perovskite solar cells. However, several other factors can be taken into consideration when progressing this work further. A study into the film crystallinity can be conducted to determine the defect density and trap state densities. These results can then be compared with similar data from previous experiments to understand the impact of our improved deposition methodologies. For the sputter deposition of ITO over the substrate, the next steps would be to incorporate these process conditions when depositing

the ITO over the perovskite material. Current studies state that the ITO deposition over the perovskite continues to damage the perovskite material due to the accelerating ITO particles. A greater process control over the deposition of ITO over the perovskite should, therefore, be initiated. One can attempt to sputter ITO over the perovskite at different RF power densities using the RF power vs Bias equation generated to estimate the best bias voltage that would enable the ITO particles to deposit over the perovskite without damaging the material. Furthermore, the stability of these devices should also be studied, since the best-performing devices need to retain their efficiency for long periods to be deemed commercially viable. The prospects of lead halide perovskite solar cells look promising, and efforts to focus the research on these particular methods would surely bring this technology a step further toward commercialization.

REFERENCES

1. Chapin, D. M., Fuller, C. S. & Pearson, G. L. A new silicon p-n junction photocell for converting solar radiation into electrical power [3]. *Journal of Applied Physics* vol. 25 Preprint at https://doi.org/10.1063/1.1721711 (1954).

2. Rau, U. & Schock, H. W. Electronic properties of Cu(In,Ga)Se2 heterojunction solar cells–recent achievements, current understanding, and future challenges. *Applied Physics A* **69**, 131–147 (1999).

3. Algora, C. *et al.* A GaAs solar cell with an efficiency of 26.2% at 1000 suns and 25.0% at 2000 suns. *IEEE Trans Electron Devices* **48**, 840–844 (2001).

4. Frerichs, R. The Photo-Conductivity of 'Incomplete Phosphors'. *Physical Review* **72**, 594–601 (1947).

5. Zuo, C. *et al.* Advances in Perovskite Solar Cells. *Advanced Science* **3**, 1500324 (2016).

6. O'Regan, B. & Grätzel, M. A low-cost, high-efficiency solar cell based on dye-sensitized colloidal TiO2 films. *Nature* **353**, 737–740 (1991).

7. Kojima, A., Teshima, K., Shirai, Y. & Miyasaka, T. Organometal Halide Perovskites as Visible-Light Sensitizers for Photovoltaic Cells. *J Am Chem Soc* **131**, 6050–6051 (2009).

8. Kim, G. Y. *et al.* Efficient Carrier Separation and Intriguing Switching of Bound Charges in Inorganic–Organic Lead Halide Solar Cells. *J Phys Chem Lett* **6**, 2355–2362 (2015).

9. Min, H. *et al.* Perovskite solar cells with atomically coherent interlayers on SnO2 electrodes. *Nature* **598**, 444–450 (2021).

10. Park, N.-G., Grätzel, M., Miyasaka, T., Zhu, K. & Emery, K. Towards stable and commercially available perovskite solar cells. *Nat Energy* **1**, 16152 (2016).

11. Castro, D., Duarte, V. C. M. & Andrade, L. Perovskite Solar Modules: Design Optimization. *ACS Omega* **7**, 40844–40852 (2022).

12. Bu, T. *et al.* Universal passivation strategy to slot-die printed SnO2 for hysteresis-free efficient flexible perovskite solar module. *Nat Commun* **9**, 4609 (2018).

13. NREL.

14. Guo, F. *et al.* A generic concept to overcome bandgap limitations for designing highly efficient multi-junction photovoltaic cells. *Nat Commun* **6**, 7730 (2015).

15. Lee, J.-W., Kim, H.-S. & Park, N.-G. Lewis Acid–Base Adduct Approach for High Efficiency Perovskite Solar Cells. *Acc Chem Res* **49**, 311–319 (2016).

16. Jiang, Q., Zhang, X. & You, J. SnO2: A Wonderful Electron Transport Layer for Perovskite Solar Cells. *Small* **14**, 1801154 (2018).

17. Hussain, T. *et al.* Experimental evidence of ion migration in aged inorganic perovskite solar cells using non-destructive RBS depth profiling. *Mater. Adv.* **3**, 7846–7853 (2022).

18. Liu, G. *et al.* Highly efficient and stable ZnO-based MA-free perovskite solar cells via overcoming interfacial mismatch and deprotonation reaction. *Chemical Engineering Journal* **431**, 134235 (2022).

19. Dong, Q., Shi, Y., Zhang, C., Wu, Y. & Wang, L. Energetically favored formation of SnO2 nanocrystals as electron transfer layer in perovskite solar cells with high efficiency exceeding 19%. *Nano Energy* **40**, 336–344 (2017).

20.	Zhu, Z. *et al.* Enhanced Efficiency and Stability of Inverted Perovskite Solar Cells Using Highly Crystalline SnO2 Nanocrystals as the Robust Electron-Transporting Layer. *Advanced Materials* **28**, 6478–6484 (2016).

21.	Rao, H.-S. *et al.* Improving the Extraction of Photogenerated Electrons with SnO2 Nanocolloids for Efficient Planar Perovskite Solar Cells. *Adv Funct Mater* **25**, 7200–7207 (2015).

22.	Xie, J. *et al.* Enhanced Electronic Properties of SnO2 via Electron Transfer from Graphene Quantum Dots for Efficient Perovskite Solar Cells. *ACS Nano* **11**, 9176–9182 (2017).

23.	Jiang, Q. *et al.* Planar-Structure Perovskite Solar Cells with Efficiency beyond 21%. *Advanced Materials* **29**, 1703852 (2017).

24.	Jiang, Q. *et al.* Enhanced electron extraction using SnO2 for high-efficiency planar-structure HC(NH2)2PbI3-based perovskite solar cells. *Nat Energy* **2**, 16177 (2016).

25.	Kim, S. *et al.* Hydrolysis-Regulated Chemical Bath Deposition of Tin-Oxide-Based Electron Transport Layers for Efficient Perovskite Solar Cells with a Reduced Potential Loss. *Chemistry of Materials* **33**, 8194–8204 (2021).

26.	Anaraki, E. H. *et al.* Highly efficient and stable planar perovskite solar cells by solution-processed tin oxide. *Energy Environ. Sci.* **9**, 3128–3134 (2016).

27.	Yoo, J. J. *et al.* Efficient perovskite solar cells via improved carrier management. *Nature* **590**, 587–593 (2021).

28.	Musil, J. Recent advances in magnetron sputtering technology. *Surf Coat Technol* **100–101**, 280–286 (1998).

29.   Window, B. Recent advances in sputter deposition. *Surf Coat Technol* **71**, 93–97 (1995).

30.   Srinivasan, K. L1(0) iron-platinum on nanocrystalline HITPERM soft magnetic underlayers for perpendicular recording media. (2004).